



Cite this: *RSC Adv.*, 2020, 10, 18400

Enhanced thermal stability of inverted perovskite solar cells by interface modification and additive strategy†

Xueqing Zheng,^{‡a} Tingming Jiang,^{‡b} Lizhong Bai,^b Xu Chen,^b Zeng Chen,^b Xuehui Xu,^b Dongdong Song,^a Xiaojian Xu,^a Bo Li^{*a} and Yang (Michael) Yang ^{*b}

Inverted perovskite solar cells (PSCs) have recently gained increasing attention because of the long operation lifetime achieved. However, bathocuproine (BCP), a commonly used buffer layer in inverted PSCs, is experimentally confirmed by us to show fast aggregation at the temperature of 85 °C, which is the protocol temperature required by the International Electrotechnical Commission (IEC) standard. This thermal instability of the BCP interfacial layer makes long-term thermal stability of inverted PSCs questionable. Simply removing or replacing it can directly lead to an inferior PCE of a device. We solve this problem by removing the BCP layer and simultaneously increasing the thickness of C₆₀, which obtains a high efficiency of 18% comparable with the device with BCP. This is possibly attributed to the extended migration path of carriers from C₆₀ to metal electrode Ag, consequently reducing the carrier accumulation at the interface. In addition to the interfacial modification, the addition of ionic liquid: BMIMBF₄ into perovskite can further improve a device's thermal stability by its effective suppression of perovskite decomposition. The devices with 0.4 mol% of BMIMBF₄ exhibit promising thermal stability by retaining 80% of their initial PCE after thermal aging of 400 h at 85 °C.

Received 10th April 2020

Accepted 5th May 2020

DOI: 10.1039/d0ra03238g

rsc.li/rsc-advances

Introduction

Metal halide perovskite solar cells (PSCs) have achieved rapid progress in the last decade due to the excellent optoelectronic properties of metal halide perovskite semiconductors such as strong light absorption, high charge mobility and long carrier diffusion lengths.^{1–12} The power conversion efficiency of single-junction PSCs has been boosted from 3.8% (ref. 13) in 2009 to 25.2% (ref. 14) at present based on the regular (n-i-p) structure. As a counterpart of the (n-i-p) structure, PSCs based on inverted (p-i-n) structure have recently gained increasing attention because of their easy fabrication, compatibility with flexible substrates and feasibility of building tandem solar cells.^{15–19} However, the PCE values of inverted PSCs are generally behind those of devices with regular structure, primarily due to severe non-radiative recombination of charge carriers.^{17,18,20} Recently, Zheng *et al.* achieved a record PCE of 22.3% (ref. 21) for inverted PSCs by using long AAL as grain and interface modifiers to favor

grain orientation and suppress trap-state density of the perovskite film, which significantly reduces the PCE gap between the regular and inverted PSCs.

Another advantage of inverted PSCs is that they have exhibited longer operational lifetime.^{22,23} Recently, Bai *et al.* introduced ionic liquid into perovskite precursor realizing operationally stable inverted PSCs with a PCE drop of only 5% under continuous one sun simulated irradiation for more than 1800 h at 70–75 °C.²² In ref. 21 with the PCE record of 22.3% for inverted PSCs, the devices maintained 100% of the initial efficiency after more than 1000 h at the maximum power point tracking under simulated AM 1.5 illumination, and lost only around 10% of their initial PCE after thermal aging of ~1020 h under temperature of 85 °C. The above two works represent the most outstanding operational stability and thermal stability of inverted PSCs. However, in the work of Bai *et al.*, the thermal aging test is carried out under 70–75 °C which is lower than the protocol (85 °C) used for commercialized photovoltaic solar module test established by International Electrotechnical Commission (IEC). This is possibly attributed to the intrinsically poor thermal stability of bathocuproine (BCP) ultrathin film which has been commonly used as buffer layer between the electron transport layer and the metal electrode in inverted structure to prevent recombination. Similarly, in the work of X. Zheng *et al.*,²¹ the authors removed BCP layer instead of a thin layer of SnO₂ via atomic layer deposition in order to conduct thermal stability of the device at 85 °C. However, the

^aDepartment of Applied Physics, College of Science, Zhejiang University of Technology, Hangzhou 310023, People's Republic of China. E-mail: libo@zjut.edu.cn

^bState Key Laboratory of Modern Optical Instrumentation, College of Optical Science and Engineering, International Research Center for Advanced Photonics, Zhejiang University, Hangzhou, Zhejiang, People's Republic of China. E-mail: yangyang15@zju.edu.cn

† Electronic supplementary information (ESI) available. See DOI: 10.1039/d0ra03238g

‡ These authors contributed equally.



replacement of BCP layer with SnO_2 sacrificed a certain PCE drop from 22.3% to 18%. It seems that whether or not to use BCP layer is a trade-off between thermal stability and efficiency.

In this paper, we focused on the model system of MAPbI_3 perovskite, and experimentally demonstrated that the device with BCP interlayer did suffer a fast degradation under thermal stressing at 85 °C, and simply removing BCP layer can cause a severe PCE loss from 18% to 6.97%. In order to solve this dilemma, we have found that getting rid of BCP and meanwhile increasing the thickness of C_{60} to 80 nm can render the champion device a comparable PCE of 18.1% with the reference device with BCP layer. As a result, the device without BCP layer exhibited almost no PCE loss after thermal aging of 12 h at 85 °C.

Based on this modification, we added 1-butyl-3-tetrafluoroborate (BMIMBF_4) ionic liquid into the perovskite precursor to further improve the device thermal stability. Consequently, our device retained 80% of its initial performance following thermal aging at 85 °C for over 400 h.

Experimental details

MAPbI_3 perovskite film preparation

The MAPbI_3 precursor solution was prepared by dissolving 0.5993 g PbI_2 (TCI) and 0.2067 g $\text{CH}_3\text{NH}_3\text{I}$ (MAI) (TCI) in 900 μL *N,N*-dimethylmethanamide (DMF) (anhydrous, Sigma-Aldrich) and 100 μL dimethyl-sulfoxide (DMSO) (anhydrous, Sigma-Aldrich). In parallel, we prepared BMIMBF_4 ionic liquids (Sigma, 97% purity) containing perovskite precursor solution by dissolving the same components in mixed solvent containing different ionic liquids (proportion and MAPbI_3 are between two thousandths and eight thousandths). The MAPbI_3 precursors were spin-coated onto ITO/ NiO_x at 4000 rpm for 50 s. 120 μL *sec*-pentanol was dropped onto the spinning substrate during the spin-coating. The condition of annealing is under 100 °C for 10 min. Several films grown on bare glass were evaporated with 25 nm C_{60} for subsequent measurement. The samples for SEM, AFM, XRD measurement were perovskite films spin-coated onto ITO/ NiO_x . The samples for UV-vis absorption were films grown on bare glass.

NiO_x film fabrication

7.4 g of nickel nitrate hexahydrate (Sinopharm Chemical Reagent, 98% purity) and 3.31 g of potassium hydroxide (Sinopharm Chemical Reagent, 85% purity) were each dissolved in 50 mL of deionized water. Then, an aqueous potassium hydroxide solution was slowly dropped into an aqueous solution of nickel nitrate. After the two were fully reacted, $\text{Ni}(\text{OH})_2$ was centrifuged. After drying $\text{Ni}(\text{OH})_2$ at 80 °C for two hours, it was placed in a high temperature furnace at 275 °C for 2 hours to obtain a NiO_x nanopowder. Prepare 25 mg mL^{-1} NiO_x solution with powder and spin-coated on cleaned ITO substrates at 3000 rpm. for 30 s and then dried at 25 °C for 30 min.

Device fabrication

The pre-patterned ITO substrates were cleaned by ultrasonication in diluted Micro-90 detergent, deionized water,

acetone, and isopropanol for 15 min, respectively. NiO_x films were coated on the cleaned ITO substrate at 3000 rpm for 30 s and then dried at 25 °C for 30 min. The MAPbI_3 perovskite films were deposited by spin-coating the precursor solution onto NiO_x film at 4000 rpm for 50 s. *sec*-Pentanol was dropped onto the spinning substrate during the spin-coating. After spin-coating, some films were annealed immediately under 100 °C for 10 min, while some were firstly stored for 15 min before annealing. Finally, some devices C_{60} (25 nm)/BCP (5 nm)/Ag (80 nm), while some devices C_{60} (80 nm)/Ag (80 nm) were sequentially deposited by thermal evaporation to complete the device fabrication.

Film and device characterization

Scanning electron microscopy (SEM) images were taken on a Hitachi SU8030 electron microscope. Atomic force microscopy (AFM) images of sample surfaces were obtained on a Cypher S Atomic Force Microscope. The absorption spectrum was measured by Agilent Carry 7000 UV-vis spectrometer. X-ray diffraction measurement was carried out by X-pert Powder. TOPAS-Academic V6 software was used for Rietveld refinements to obtain the lattice parameters. The background and peak shapes were fit using a shifted Chebyshev function with eight parameters and a Pseudo-Voigt function (TCHZ type), respectively. Current density-voltage (J - V) characteristics were measured under AM 1.5G light (1000 W m^{-2}) using the xenon arc lamp of a Class A solar simulator. Light intensity was calibrated using an Newport-calibrated mono crystalline Si diode. The Keithley 2400 source meter was used for I - V measurement. External quantum efficiency (EQE) was characterized with an integrated system (QER3018) from EnliTech. Samples were kept in a N_2 filled cell at room temperature for all optical measurements.

Results and discussion

The architecture of our standard inverted PSCs is shown in Fig. 1a, which consists of glass/ITO/ NiO_x / MAPbI_3 / C_{60} (25 nm)/BCP (5 nm)/Ag (100 nm). The champion device gives a high PCE of 18.04% with a V_{oc} of 0.98 V, J_{sc} of 22.21 mA cm^{-2} and FF of 0.83 under reverse direction, shown in Fig. 1b, and a negligible hysteresis is observed. Fig. S1† shows a histogram of PCE values of 40 devices from different batches, which indicates a high reproducibility of our device fabrication. The J - V curves of device before and after heating at 85 °C are placed in Fig. 1c. It can be observed that the PCE of the device has rapidly dropped to 12.1% from its initial value of 17.1% only for 12 h of thermal aging under 85 °C. In order to understand the factors triggering such rapid device degradation, the XRD measurements for the perovskite films deposited on pristine glass before and after thermal aging have been carried out as shown in Fig. 1d. The XRD pattern of the perovskite film after 12 h of thermal aging at 85 °C remains almost unaltered with that of perovskite film without heating treatment. This result rules out the possibility of perovskite film degradation within 12 h of thermal heating. Therefore, we conjecture that the thin



interlayer BCP is likely to be associated with this degradation during the thermal aging process. The AFM images of the BCP film (5 nm) grown on pristine glass before and after thermal aging are shown in Fig. 1e and f. The BCP film after 12 h of heating under 85 °C has exhibited a high level of clustering and aggregation²⁴ which is clearly attributed to thermal heating. Differential Scanning Calorimetry (DSC) thermograph of BCP powder is shown in Fig. S2† which exhibits a slight endotherm peak at about 84.2 °C possibly resulting in the BCP clustering. The appearance of BCP molecule clustering has resulted the root-mean-square roughness of the film increasing from 6.68 nm before thermal aging to 10.42 nm after thermal aging. The increased BCP film roughness can potentially lead to a certain degree of electrical shunting²⁴ of the device that consequently hampers the device performance.

The above results have experimentally demonstrated that the BCP molecules undergo aggregation under thermal environment under 85 °C and causes a fast device degradation. Therefore, we tried to simply remove the BCP buffer layer

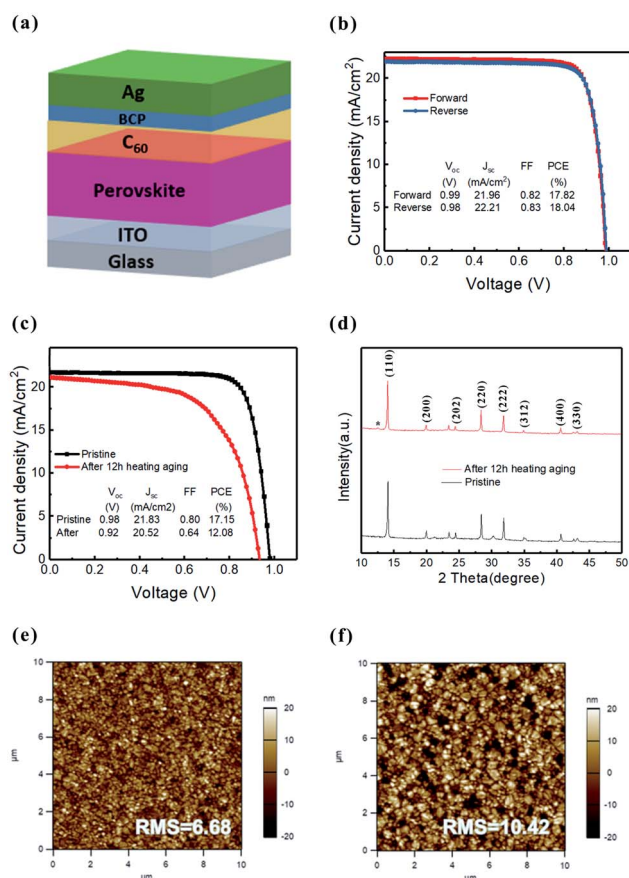


Fig. 1 (a) Schematic diagram of our standard p-i-n device structure; (b) J - V curves of the best-performing device under forward and reverse scans with photovoltaic parameters inserted, respectively; (c) histogram of PCEs of 40 devices; (d) J - V curves of devices before and after thermal aging for 12 h under 85 °C AFM images of BCP thin film (5 nm) deposited on glass before; (e) and after (f) thermal aging for 12 h under 85 °C.

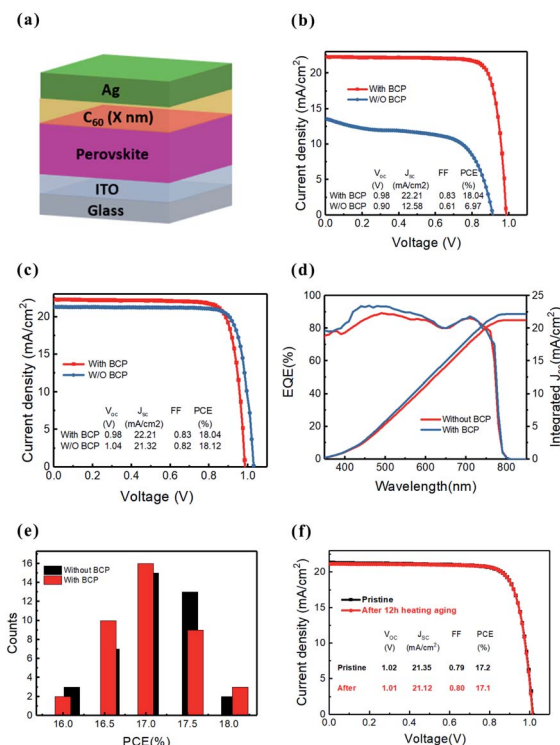


Fig. 2 (a) Schematic diagram of the device structure without BCP buffer layer and varied thickness of C_{60} layer; (b) J - V curves of (C_{60} thickness: 25 nm for both cases); (c) J - V curves of the standard device with BCP layer (5 nm) and C_{60} layer (25 nm), and devices without BCP layer and with C_{60} layer of 80 nm; (d) external quantum efficiency (EQE) spectra and integrated J_{sc} of the standard device with BCP layer (5 nm) and C_{60} layer (25 nm), and devices without BCP layer and with C_{60} layer of 80 nm over 40 cells; (e) histograms of PCEs of standard device with BCP layer (5 nm) and C_{60} layer (25 nm), and device without BCP layer and with C_{60} layer of 80 nm over 40 cells; (f) J - V curves of device without BCP layer and with C_{60} layer of 80 nm before and after thermal aging of 12 h under 85 °C.

completely as shown in Fig. 2a without any other changes compared with our standard device in Fig. 1a.

However, as shown in Fig. 2b the PCE of the device without BCP layer has evidently dropped to 10% compared with 18.04% of our standard device with BCP buffer layer of 5 nm, which are in accordance with the previous reports:^{25–27} A Schottky barrier will be formed at the interface when n-type semiconductor C_{60} is directly contacted with the metal electrode Ag which can give rise to larger interface resistance and charge accumulation at

Table 1 Characteristics of PSCs of solar cell ITO/ NiO_x (20 nm)/perovskite (500 nm)/ C_{60} (X nm)/Ag (100 nm) with X value under illumination

X (nm)	J_{sc} (mA cm ⁻²)	V_{oc} (V)	FF	PCE (%)
25	12.58	0.90	0.61	6.97
60	21.06	1.02	0.82	17.60
80	21.23	1.04	0.82	18.12
100	20.58	1.04	0.81	17.33



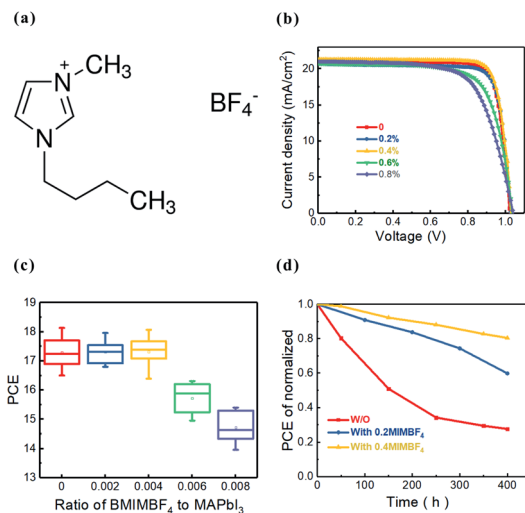


Fig. 3 (a) Chemical structure of the ionic liquid BMIMBF₄; (b) current density–voltage (*J*–*V*) curves of device with the configuration of ITO/NiO_x (20 nm)/perovskite (500 nm)/C₆₀ (80 nm)/Ag (100 nm) containing different concentration of BMIMBF₄ from 0.2 to 0.8 mol% with respect to the stoichiometric amount of perovskite MAPbI₃; (c) statistics of device PCE using perovskite precursors with a BMIMBF₄ concentration ranging from 0.2% to 0.8%; (d) thermal stability of devices with a varying concentration of BMIMBF₄ at a fixed temperature of 85 °C in a N₂ atmosphere.

Table 2 Photovoltaic parameters of PSCs: ITO/NiO_x (20 nm)/perovskite (500 nm)/C₆₀ (80 nm)/Ag (100 nm) with varying content of BMIMBF₄

Ratio	<i>J</i> _{sc} (mA cm ^{−2})	<i>V</i> _{oc} (V)	FF	PCE (%)
0	21.32	1.04	0.82	18.13
0.2 mol%	21.01	1.03	0.83	17.96
0.4 mol%	21.46	1.04	0.81	18.07
0.6 mol%	21.15	1.04	0.74	16.31
0.8 mol%	21.18	1.05	0.68	15.20

the interface. The introduction of BCP block layer between C₆₀ and Ag can change the Schottky into an ohmic contact and finally contribute to the improvement of device performance. It is noteworthy to point out that the thickness of C₆₀ is just 25 nm in our standard device without BCP layer so that the migration distance of photo-generated electrons from C₆₀ to Ag is shorter which can possibly lead to a large degree of charge accumulation at the interface because the electrons are not able to transport to the Ag in time due to the existence of Schottky barrier. As a result, a severe recombination is likely to occur at the interface resulting in the poor device performance. Therefore, we proposed to increase the thickness of C₆₀ to lengthen the path of electrons from to Ag, which may mitigate the accumulation of carriers at the interface.

The photovoltaic parameters of devices with different thickness of C₆₀ are shown in Table 1. It can be seen that the PCEs of the devices gradually increase as the C₆₀ thickness increases from 25 nm to 80 nm. However, the device efficiency

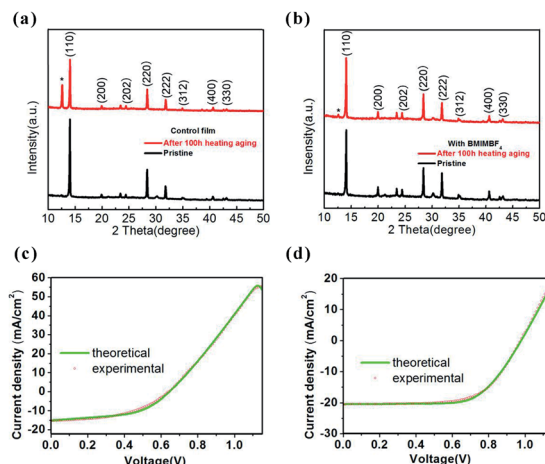


Fig. 4 (a and b) XRD patterns of pristine and aged samples of control film and film containing BMIMBF₄ (0.4%) on NiO_x/ITO coated glass substrates after 100 h under 85 °C; (c and d) the modeled and experimental *J*–*V* characteristics of PSCs without and with BMIMBF₄ after 400 h heating aging with 85 °C (in a glove box filled with nitrogen).

starts to decrease when the thickness of C₆₀ reaches to 100 nm, which is possibly attributed to the too thick layer of C₆₀ resulting in a severe carrier recombination during the transportation of electrons through C₆₀ layer. Based on our results, the increase of C₆₀ thickness in fact contributes to the improvement of the device performance without the BCP blocking layer. The champion device without BCP achieves PCE of 18.12% based on the C₆₀ thickness of 80 nm as shown in Fig. 2c, which is comparable with that of the standard device with BCP layer. And the hysteresis of the device is almost negligible shown in Fig. S3.† It is worth to mention that the *V*_{oc} of the champion device with C₆₀ thickness of 80 nm and without BCP layer is slightly larger than that of device with BCP (5 nm) and C₆₀ (25 nm) layer as seen in Fig. 2c, which is still likely due to the reduced carrier accumulation at the interface of C₆₀ and Ag benefiting from the longer migration of electron within C₆₀ layer. By contrast, the *J*_{sc} of device without BCP is relatively lower than that of device with BCP layer since the existence of BCP buffer layer can anyhow lower down the Schottky barrier and can offer a higher carrier generation yield leading to a higher *J*_{sc}.^{24–26} The Fig. 2d shows the EQE spectra of solar cells with and without BCP layer. Their integrated *J*_{sc} values from the EQE spectra are determined to be respectively, which match well with their *J*_{sc} obtained from the *J*–*V* curves. Fig. 2e exhibits the PCEs histograms of devices with and without BCP layer over 40 samples for each type, which demonstrate a significant overlap. This indicates that our strategy to remove BCP and improve the C₆₀ thickness has reliably achieved the device PCE comparable with the standard device with BCP layer.

We proceed to conduct the thermal stability test to the device without BCP layer under 85 °C for 12 h as displayed in Fig. 2f. No PCE loss is observed after thermal aging of 12 h at 85 °C. The removal of BCP layer and increasing the thickness of C₆₀ has not only achieved comparable device PCE with the standard device



Table 3 The experimental J – V characteristics of PSCs without and with BMIMBF₄ after 400 h heating under 85 °C

Thermal aging of 400 h	γ ($10^7 \text{ m}^3 \text{ s}^{-1}$)	R_s (10^{-4} ohm m^2)	R_{sh} (ohm m^2)
With BMIMBF ₄	4.8	7.46	2.7×10^4
W/O BMIMBF ₄	1.7×10^3	6.75	1.4×10^{-4}

with BCP layer, but also solved the instability issue of BCP molecules under 85 °C heating which lays the foundation of further improving the thermal stability of our inverted PSCs.

Introducing additives to perovskite is one of the most effective methods to improve PSCs stability.^{28,29} To further improve the thermal stability of the inverted PSCs, an ionic liquid 1-butyl-3-methylimidazolium tetrafluoroborate with the chemical structure shown in Fig. 3a (BMIMBF₄ in short) is incorporated into the perovskite film based on the study²² of S. Bai *et al.* The J – V curves of the devices with BMIMBF₄ concentration varying from 0 to 0.8 mol% are exhibited in Fig. 3b, the corresponding statistics of PCE is shown in Fig. 3c. The PCEs of the devices with BMIMBF₄ concentration of 0.2 mol% and 0.4 mol% remain almost unchanged with respect to the control device without BMIMBF₄ addition. And there is no evident hysteresis caused by the introduction of BMIMBF₄ shown in Fig. S4,[†] in contrast to the work of Bai *et al.*, in which significant hysteresis occurred after the addition of BMIMBF₄. In addition, the morphology and crystallization of perovskite films with and without BMIMBF₄ also show no obvious changes from the observations of SEM images and XRD patterns in Fig. S5.[†] However, to further increase the concentration of BMIMBF₄ over 0.4 mol% results in decreased PCEs of the devices mainly reflected in the FF loss. After 400 h of thermal aging at 85 °C shown in Fig. 3d, the control device without BMIMBF₄ exhibits a fast degradation and only retains less than 30% of its initial PCE, while the devices with BMIMBF₄ of 0.2 and 0.4 mol% retain 60% and 80% of their initial values, respectively. It indicates that the optimal concentration of BMIMBF₄ is about 0.4 mol% which endows the corresponding device with the best performance against thermal aging at 85 °C (Table 2).

To elucidate the mechanism of BMIMBF₄ for enhancing the thermal stability of the devices, we carried out thermal stability test to the perovskite films without (as control) and with BMIMBF₄ addition for 100 h under 85 °C heating, and the XRD patterns of the corresponding perovskite films are recorded shown in Fig. 4a and b. From the XRD pattern of the control film, a strong peak at 14.2° appeared which is indexed as the peak of PbI₂. The appearance of PbI₂ typically originates from the decomposition of perovskite MAPbI₃ caused by the long-term heating pressure according to previous studies.^{30–34} The MAPbI₃ perovskites can decompose to form PbI₂ at elevated temperatures even without exposure to oxygen and water consequently resulting in the PCE decline of the MAPbI₃ based PSCs. However, the PbI₂ peak of the perovskite film with BMIMBF₄ addition is quite small which demonstrates that the BMIMBF₄ can effectively suppress the decomposition of MAPbI₃ perovskites at high temperatures accountable for the improved thermal stability of the devices with BMIMBF₄ addition.

We employed a modified detailed balance mode^{10,15,35} to understand the PCE loss mechanism of the devices caused by the decomposition of MAPbI₃ perovskites under long-term thermal aging from the point view of device physics. This model is governed by the formula below:

$$J = \frac{V - JR_s}{R_{sh}} + J_n(V - JR_s) + J_r(V - JR_s) - J_p$$

in which, V is the applied voltage of a solar cell. J_p is the photocurrent. J_r and J_n are the current losses resulting from radiative and nonradiative recombination. More details about the formula and physical meanings can be found elsewhere. Given a J – V curve, the curve can be modeled to retrieve three primary parameters including the nonradiative recombination rate γ , the series resistance R_s and the shunt resistance R_{sh} . R_s is related to the ohmic loss at the contact, carrier transport layers, as well as the heterojunction interfaces between the perovskite and carrier transport layers. R_{sh} is an indication of the defects and pinhole-induced current leakage. Fig. 4c and d shows the modeled and experimentally measured J – V curves of PSCs with and without 0.4% BMIMBF₄ after thermal aging of 400 h under 85 °C heating. Table 3 shows the retrieved characteristic parameters from measured J – V curves. It can be seen that the nonradiative recombination rate γ for device with BMIMBF₄ is 350 times lower than that of device without BMIMBF₄, which indicates much lower carrier recombination rate for the whole device including not only the perovskite bulk but also the interfaces between perovskite and carrier transport layers. In addition, the much larger R_{sh} of device with BMIMBF₄ manifests lower interfacial ohmic loss and defect-induced current leakage. These results are in good accordance with the less degree of perovskite decomposition by the assist of BMIMBF₄ after long time thermal aging directly revealed by the small intensity of PbI₂ peak in the XRD patterns.

Conclusions

In summary, we have experimentally demonstrated that the BCP buffer commonly used in inverted PSCs undergoes molecule clustering and aggregation rapidly under thermal aging at 85 °C leading to a fast degradation of device performance which are impossible to fulfill the requirement of long-term thermal stability. But simply removing the BCP layer results in an inferior PCE of the solar cells. We have found that the PCEs of the devices without BCP buffer layer gradually improves as the thickness increase of electron transport layer (C_{60} used in our case), which is possibly due to extended migration path of carriers from C_{60} to metal electrode Ag consequently reducing the carrier accumulation at the interface. The PCE of champion



device without BCP layer is comparable with the standard device with BCP layer. An optimal amount of BMIMBF₄ is added into perovskite precursor to further improve the device thermal stability due to its effective inhibition of MAPbI₃ perovskite decomposition evidenced from the suppressed PbI₂ XRD peak as a typical decomposition byproduct. Finally, the device with 0.4 mol% BMIMBF₄ retains 80% of its initial efficiency after 400 h of thermal aging at 85 °C, which is one of the best results for inverted PSCs in terms of thermal stability. This work represents promising guidelines for commercialization of PSCs in thermal stability test at protocol temperature 85 °C in light of device structure modification and perovskite additive strategy.

Conflicts of interest

There are no conflicts to declare.

Acknowledgements

The authors want to acknowledge the financial support received from National Key Research and Development Program of Zhejiang Province (2018C04SA170313); Outstanding Youth fund of Zhejiang Natural Science Foundation of China (LR18F050001); Natural Science Foundation of China (61804134); Zhejiang Provincial Natural Science Foundation of China under Grant No. LY14F040003.

References

- Q. Dong, Y. Fang, Y. Shao, P. Mulligan, J. Qiu, L. Cao and J. Huang, Solar cells. Electron-hole diffusion lengths > 175 μm in solution-grown CH₃NH₃PbI₃ single crystals, *Science*, 2015, **347**, 967–970.
- M. Liu, M. B. Johnston and H. J. N. Snaith, Efficient planar heterojunction perovskite solar cells by vapour deposition, *Nature*, 2013, **501**, 395–398.
- J. Burschka, N. Pellet, S.-J. Moon, R. Humphry-Baker, P. Gao, M. K. Nazeeuruddin and M. Grätzel, Sequential deposition as a route to highperformance perovskite-sensitized solar cells, *Nature*, 2013, **499**, 316–319.
- M. Abdi-Jalebi, Z. Andaji-Garmaroudi, S. Cacovich, C. Stavrakas, B. Philippe, J. M. Richter, M. Alsari, E. P. Booker, E. M. Hutter and A. J. Pearson, Maximizing and stabilizing luminescence from halide perovskites with potassium passivation, *Nature*, 2018, **555**, 497–501.
- T. Jiang, Z. Chen, X. Chen, X. Chen, X. Xu, T. Liu, L. Bai, D. Yang, D. Di, W. E. Sha, H. Zhu and Y. Yang, Power Conversion Efficiency Enhancement of Low-Bandgap Mixed Pb–Sn Perovskite Solar Cells by Improved Interfacial Charge Transfer, *ACS Energy Lett.*, 2019, **4**, 1784.
- D. Bi, C. Yi, J. Luo, J.-D. Décoppet, F. Zhang, S. M. Zakeeruddin, X. Li, A. Hagfeldt and M. Grätzel, Polymer-templated nucleation and crystal growth of perovskite films for solar cells with efficiency greater than 21%, *Nat. Energy*, 2016, **1**, 1.
- H. Tsai, W. Nie, J.-C. Blancon, C. C. Stoumpos, R. Asadpour, B. Harutyunyan, A. J. Neukirch, R. Verduzco, J. J. Crochet and S. Tretiak, High-efficiency two-dimensional Ruddlesden-Popper perovskite solar cells, *Nature*, 2016, **536**, 312–316.
- X. Li, D. Bi, C. Yi, J.-D. Décoppet, J. Luo, S. M. Zakeeruddin, A. Hagfeldt and M. Grätzel, A vacuum flash-assisted solution process for high-efficiency large-area perovskite solar cells, *Science*, 2016, **353**, 58–62.
- Q. Jiang, Y. Zhao, X. Zhang, X. Yang, Y. Chen, Z. Chu, Q. Ye, X. Li, Z. Yin and J. You, Surface passivation of perovskite film for efficient solar cells, *Nat. Photonics*, 2019, **13**, 460–466.
- T. Jiang, Z. Chen, X. Chen, T. Liu, X. Chen, W. E. Sha, H. Zhu and Y. Yang, Realizing High Efficiency over 20% of Low-Bandgap Pb–Sn-Alloyed Perovskite Solar Cells by *In Situ* Reduction of Sn⁴⁺, *Sol. RRL*, 2019, 1900467.
- D. Zhao, C. Chen, C. Wang, M. M. Junda, Z. Song, C. R. Grice, Y. Yu, C. Li, B. Subedi and N. J. Podraza, Efficient two-terminal all-perovskite tandem solar cells enabled by high-quality low-bandgap absorber layers, *Nat. Energy*, 2018, **3**, 1093–1100.
- R. Zhuang, X. Wang, W. Ma, X. Wu, X. Chen, L. Tang, H. Zhu, J. Liu, L. Wu, W. Zhou, X. Liu and Y. Yang, Highly sensitive X-ray detector made of layered perovskite-like (NH₄)₃Bi₂I₉ single crystal with anisotropic response, *Nat. Photonics*, 2019, **13**, 602–608.
- A. Kojima, K. Teshima, Y. Shirai and T. Miyasaka, Organometal halide perovskites as visible-light sensitizers for photovoltaic cells, *J. Am. Chem. Soc.*, 2009, **131**, 6050–6051.
- National Renewable Energy Laboratory, *Best research-cell efficiencies*, 2019, www.nrel.gov/pv/assets/pdfs/pv-efficiency-chart.20190103.pdf.
- K. A. Bush, A. F. Palmstrom, J. Y. Zhengshan, M. Boccard, R. Cheacharoen, J. P. Mailoa, D. P. McMeekin, R. L. Hoyer, C. D. Bailie and T. Leijtens, 23.6%-efficient monolithic perovskite/silicon tandem solar cells with improved stability, *Nat. Energy*, 2017, **2**, 17009.
- W. Chen, Y. Wu, Y. Yue, J. Liu, W. Zhang, X. Yang, H. Chen, E. Bi, I. Ashraf and M. Grätzel, Efficient and stable large-area perovskite solar cells with inorganic charge extraction layers, *Science*, 2015, **350**, 944.
- D. Luo, W. Yang, Z. Wang, A. Sadhanala, Q. Hu, R. Su, R. Shivanna, G. F. Trindade, J. F. Watts and Z. Xu, Enhanced photovoltage for inverted planar heterojunction perovskite solar cells, *Science*, 2018, **360**, 1442–1446.
- X. Zheng, B. Chen, J. Dai, Y. Fang, Y. Bai, Y. Lin, H. Wei, X. C. Zeng and J. Huang, Defect passivation in hybrid perovskite solar cells using quaternary ammonium halide anions and cations, *Nat. Energy*, 2017, **2**, 17102.
- J. Zhao, X. Zheng, Y. Deng, T. Li, Y. Shao, A. Gruverman, J. Shield and J. Huang, Is Cu a stable electrode material in hybrid perovskite solar cells for a 30-year lifetime?, *Energy Environ. Sci.*, 2016, **9**, 3650–3656.
- S.-H. Turren-Cruz, A. Hagfeldt, M. Saliba, S.-H. Turren-Cruz, A. Hagfeldt and M. Saliba, Methylammonium-free, high-performance, and stable perovskite solar cells on a planar architecture, *Science*, 2018, **362**, 449–453.
- X. Zheng, Y. Hou, C. Bao, J. Yin, F. Yuan, Z. Huang, K. Song, J. Liu, J. Troughton and N. Gasparini, Managing grains and



- interfaces *via* ligand anchoring enables 22.3%-efficiency inverted perovskite solar cells, *Nat. Energy*, 2020, **5**, 131.
- 22 S. Bai, P. Da, C. Li, Z. Wang, Z. Yuan, F. Fu, M. Kawecki, X. Liu, N. Sakai and J. T.-W. Wang, Planar perovskite solar cells with long-term stability using ionic liquid additives, *Nature*, 2019, **571**, 245–250.
 - 23 S. Yang, S. Chen, E. Mosconi, Y. Fang, X. Xiao, C. Wang, Y. Zhou, Z. Yu, J. Zhao and Y. Gao, Stabilizing halide perovskite surfaces for solar cell operation with wide-bandgap lead oxysalts, *Science*, 2019, **365**, 473–478.
 - 24 F. Jafari, B. R. Patil, F. Mohtaram, A. L. F. Cauduro, H.-G. Rubahn, A. Behjat and M. Madsen, Inverted organic solar cells with non-clustering bathocuproine (BCP) cathode interlayers obtained by fullerene doping, *Sci. Rep.*, 2019, **9**, 1.
 - 25 C. Chen, S. Zhang, S. Wu, W. Zhang, H. Zhu, Z. Xiong, Y. Zhang and W. Chen, Effect of BCP buffer layer on eliminating charge accumulation for high performance of inverted perovskite solar cells, *RSC Adv.*, 2017, **7**, 35819.
 - 26 N. Shibayama, H. Kanda, T. W. Kim, H. Segawa and S. Ito, Design of BCP buffer layer for inverted perovskite solar cells using ideal factor, *APL Mater.*, 2019, **7**, 031117.
 - 27 C. He, F. Zhang, X. Zhao, C. Lin and M. Ye, Interface Engineering of BCP Buffer Layers in Planar Heterojunction Perovskite Solar Cells With NiO_x Hole Transporting Layers, *Front. Phys.*, 2018, **6**, 99.
 - 28 L. Wang, H. Zhou and J. Hu, A Eu³⁺-Eu²⁺ ion redox shuttle imparts operational durability to Pb-I perovskite solar cells, *Science*, 2019, **366**, 749–753.
 - 29 M. Kim, G. Kim and T. K. Lee, Methylammonium chloride induces intermediate phase stabilization for efficient perovskites solar cells, *Joule*, 2019, **3**, 2179–2192.
 - 30 N.-K. Kim, Y. H. Min, S. Noh, E. Cho, G. Jeong, M. Joo, S.-W. Ahn, J. S. Lee, S. Kim and K. Ihm, Investigation of Thermally Induced Degradation in CH₃NH₃PbI₃ Perovskite Solar Cells using *In situ* Synchrotron Radiation Analysis, *Sci. Rep.*, 2017, **7**, 4645.
 - 31 B. Conings, J. Drijkoningen, N. Gauquelin, A. Babayigit, J. D'Haen, L. D'Olieslaeger, A. Ethirajan, J. Verbeeck, J. Manca and E. Mosconi, Intrinsic Thermal Instability of Methylammonium Lead Trihalide Perovskite, *Adv. Energy Mater.*, 2015, **5**, 1500477.
 - 32 G. Divitini, S. Cacovich, F. Matteocci, L. Cinà, A. Di Carlo and C. Ducati, In situ observation of heat-induced degradation of perovskite solar cells, *Nat. Energy*, 2016, **1**, 15012.
 - 33 B. Philippe, B.-W. Park, R. Lindblad, J. Oscarsson, S. Ahmadi and E. M. J. Johansson, Chemical and electronic structure characterization of lead halide perovskites and stability behavior under different exposures—a photoelectron spectroscopy investigation, *Chem. Mater.*, 2015, **27**, 1720–1731.
 - 34 E. J. Juarez-Perez, L. K. Ono, M. Maeda, Y. Jiang, Z. Hawash and Y. Qi, Photodecomposition and thermal decomposition in methylammonium halide lead perovskites and inferred design principles to increase photovoltaic device stability, *J. Mater. Chem. A*, 2018, **6**, 9604.
 - 35 W. E. Sha, H. Zhang, Z. S. Wang, H. L. Zhu, X. Ren, F. Lin, A. K. Y. Jen and W. C. Choy, Quantifying Efficiency Loss of Perovskite Solar Cells by a Modified Detailed Balance Model, *Adv. Energy Mater.*, 2018, **8**, 1701586.

